Available online at website: https://journal.bcrec.id/index.php/bcrec

Bulletin of Chemical Reaction Engineering & Catalysis, 21 (3) 2026, 553-568

Original Research Article

Visible-Light Photocatalytic Degradation of Metronidazole Using Bismuth Oxide-Doped Erbium Oxide Anchored Graphene Oxide Nanocomposites: Kinetics and Mechanism

Nada D. Ali[1], Usama A. Saed[1*], Waqar A. Abdulnabi[1], Zeyad Zeitoun[2,3*]

[1]*Chemical Engineering Department, College of Engineering, Al-Nahrain University, Baghdad, Iraq.*
[2]*Department of Engineering and Computer Science, McNeese State University, Lake Charles, LA, United States.*
[3]*Chemical Engineering Department, Faculty of Engineering, Alexandria University, Alexandria, Egypt.*

Received: 25th January 2026; Revised: 29th March 2026; Accepted: 30th March 2026
Available online: 1st April 2026; Published regularly: October 2026

Abstract

Metronidazole (MNZ) is a persistent pharmaceutical contaminant that resists conventional wastewater treatment. In this work, a visible-light-active Bi_2O_3–Er_2O_3/graphene oxide (GO) nanocomposite was synthesized by a co-precipitation method. This nanocomposite was evaluated for the photocatalytic degradation of MNZ in aqueous solution. Structural and optical characterization (XRD, FTIR, SEM, TEM, BET, PL, and UV–Vis DRS) confirmed the successful anchoring of Bi_2O_3–Er_2O_3 nanoparticles onto GO sheets. That resulted in improved visible-light absorption and blocked charge-carrier recombination. The composite containing 20 wt% GO showed the highest photocatalytic activity. It achieved near-complete MNZ removal under exposure to visible light. The improved performance was attributed to the combined effects of many factors. Those include Bi_2O_3–Er_2O_3-induced visible-light response, Er_2O_3-assisted charge trapping, and efficient electron transport through GO. The study included examining the effects of many factors. Those included the solution pH, catalyst dosage, initial MNZ concentration, and GO content. Optimal degradation was found in alkaline conditions. The catalyst was found to be stable and reusable. Therefore, it has high potential for sustainable antibiotic removal from wastewater.

Keywords: Wastewater Treatment; Adsorption; Graphene Oxide; Metronidazole; Material Characterization

How to Cite: Ali, N. D., Saed, U. A., Abdulnabi, W. A., Zeitoun, Z. (2026). Visible-Light Photocatalytic Degradation of Metronidazole Using Bismuth Oxide-Doped Erbium Oxide Anchored Graphene Oxide Nanocomposites: Kinetics and Mechanism. *Bulletin of Chemical Reaction Engineering & Catalysis*, 21 (3), 553-568. (DOI: 10.9767/bcrec.20651)

Permalink/DOI: https://doi.org/10.9767/bcrec.20651

1. Introduction

Pharmaceutical pollutants have emerged as a critical class of environmental contaminants. They are so critical since they are released continuously into the environment. They are resistant to degradation, and have the potential to cause antimicrobial resistance [1]. Among these is Metronidazole (MNZ). That is a synthetic nitroimidazole antibiotic. It is widely used for treating anaerobic bacterial and protozoal infections. It has been found in municipal wastewater, hospital effluents, and even natural water. MNZ is chemically stable and resistant to biodegradation. That makes it resistant to conventional wastewater treatment processes. Its accumulation causes ecological hazards. It can also disturb water microbial communities. Therefore, developing efficient, sustainable, and sunlight-driven degradation strategies for MNZ has become an urgent environmental priority [2]. Advanced oxidation processes (AOPs) have become prominent as effective methods for degrading recalcitrant organic pollutants. Among this class of pollutants is pharmaceuticals. These processes work by generating highly reactive oxidative species, in-situ. These species include hydroxyl radicals (•OH) and superoxide radicals (O_2•$^-$). They oxidize organic contaminants to harmless end-products like CO_2 and H_2O. Among various AOPs, semiconductor-based

* Corresponding Authors.
Email: usama.a.sead@nahrainuniv.edu.iq (U.A. Saed)
zzeitoun@mcneese.edu (Z. Zeitoun)

photocatalysis is environmentally gentle. It uses light energy to activate semiconductor materials. Classical photocatalysts such as TiO_2 and ZnO are effective under ultraviolet (UV) exposure [3]. They showed limited solar-light utilization, however. That is due to their wide bandgaps (~3.2 eV). Consequently, the development of visible-light-responsive photocatalysts has become a research frontier to harness the full potential of sunlight for wastewater treatment [4,5].

Bismuth(III) oxide is a p-type semiconductor notable for its narrow bandgap and rich defect chemistry. It exists in several polymorphs (e.g. monoclinic α-, tetragonal β-, and cubic γ-phases) with bandgaps on the order of 2.6 - 2.9 eV. For example, γ- Bi_2O_3 nanoparticles have an observed direct bandgap of ~2.9 eV (absorption edge ~434 nm), allowing absorption of visible blue light. The valence band of Bi_2O_3 is derived largely from O 2p orbitals, and its conduction band from Bi 6p orbitals; the stereoactive $6s^2$ lone pair on Bi^{3+} also influences its electronic structure. In photocatalysis, Bi_2O_3 can generate oxidizing holes capable of producing •OH radicals. However, pure Bi_2O_3 often suffers from rapid electron-hole recombination and limited light harvesting on its own [6].

To overcome these issues, Bi_2O_3 is frequently combined with other materials. Doping or compositing with narrower-bandgap semiconductors extends light absorption, while heterojunctions improve charge separation. For instance, doping ZnO with Bi_2O_3 creates an n–p junction: the Bi_2O_3 narrows ZnO's effective bandgap and sensitizes it to visible light. A ternary ZnO–Bi_2O_3/GO composite demonstrated this: it achieved 99.6 % degradation of methylene blue under visible irradiation, largely because the GO sheet stabilized the particles and acted as an electron sink to suppress recombination. In that system, GO's presence "enhances the stability of ZnO - Bi_2O_3 and reduces the recombination of charge carriers," while Bi_2O_3 doping "excites the absorption of visible light" in ZnO [7].

Beyond ZnO, Bi_2O_3 is often used in multi-component oxides. For example, co-doping Bi_2O_3 with rare-earth oxides has shown promise. A solid-solution system $(Er_2O_3)_x$ $(Yb_2O_3)_\gamma$ $(Bi_2O_3)_{1-x-\gamma}$ demonstrated complete degradation of a model dye (crystal violet) in 30 minutes under visible light when optimally doped [8]. In that ternary, Er^{3+}/Yb^{3+} co-doping likely introduced up conversion and multiple energy levels, creating "synergic effects" in Bi_2O_3's photocatalysis. Similarly, a CuO - Bi_2O_3 nanocomposite achieved 95.6 % dye degradation (far above either CuO or Bi_2O_3 alone) [9]. These results confirm that Bi_2O_3 serves as an excellent partner in heterostructures: it provides visible-light absorption and reactive holes, while its combination with other materials greatly boosts overall activity.

Erbium(III) oxide is a rare-earth semiconductor with distinctly different behavior. It has a very wide intrinsic bandgap (≈5.3 eV), so it does not absorb visible light on its own. For instance, calculations give the Er_2O_3 valence band ~8.26 eV below vacuum and a bandgap of 5.3 eV, implying a conduction band >2.9 eV below vacuum – too deep for visible excitation. Consequently, pure Er_2O_3 cannot directly drive photochemical reactions under sunlight. The value of Er_2O_3 in photocatalysis lies instead in its lanthanide 4f electronic structure. Trivalent Er^{3+} ions show up conversion luminescence. The way is that they absorb two or more low-energy photons and re-emit a single higher-energy photon. Those low-energy photons could be infrared or visible light photons. This makes Er_2O_3 an energy converter. Therefore, the photocatalyst's response is extended into the IR or the deep red region. For example, introducing Er_2O_3 into a $ZnIn_2S_4$ semiconductor created an S-scheme heterojunction. The performance of this was largely improved under exposure to sun light [10]. In that Er_2O_3/$ZnIn_2S_4$ system, the up-conversion property of Er^{3+} "expanded the light response range," enabling use of sub-band-gap photons. Simultaneously, engineered oxygen vacancies improved charge separation, and an internal electric field at the junction further accelerated carrier transfer. The result was exceptional: compared to pristine Er_2O_3 or $ZnIn_2S_4$, the heterojunction produced ~560× and ~430× greater CO_2-to-CH_4 conversion under light [10].

Thus, Er_2O_3 contributes mainly through up conversion and as a dopant/heterojunction component, rather than by its own UV absorption. By converting IR photons to visible and by forming energetic 4f levels that trap or transfer carriers, Er_2O_3 can significantly boost the efficiency of composite photocatalysts. In a Bi_2O_3-based composite, for example, Er^{3+}/Yb^{3+} co-doping enabled near-complete dye degradation [8]. In a GO-supported material, Er_2O_3 would similarly provide up conversion centers.

Graphene oxide is a two-dimensional carbon material rich in oxygen functional groups. Its photochemistry-related properties include high electrical conductivity (especially after partial reduction), abundant surface chemistry, and good dispersibility in water [11]. These attributes make GO an excellent component in hybrid photocatalysts. The oxygenated groups offer adsorption sites for polar pollutants. This can produce strong interactions (e.g. hydrogen bonding) with organic molecules [12-14]. The result would be to concentrate those groups near the photocatalytic sites. The conjugated sp^2 carbon network gives GO (and reduced GO) conductivity similar to that of metals. As result it becomes able to transport electrons quickly.

Therefore, GO often serves as an electron sink or conductive scaffold. The function of this scaffold is taking photogenerated electrons from a semiconductor [15]. Thus, recombination is suppressed. That is, GO can act as a "cross-linked framework" or template for anchoring semiconductor particles. It also act as a many-sided intermediary in charge transfer [11, 16].

The role of those GO was stressed in the literature. For example, in the ZnO - Bi_2O_3/GO composite, the GO sheet obviously improved photocatalytic outcomes. It improved composite stability and reduced charge recombination. That allowed almost complete dye degradation under visible light [7]. In general, the literature notes that incorporation of GO (or partially reduced GO) into photocatalysts "enhances the photocatalytic efficiency" by improving charge separation and providing extra reaction pathways [11]. Moreover, GO acts as a two-dimensional growth substrate for the semiconductor, promoting small crystal size and high dispersion. In the context of rare-earth oxides, GO has also been used: for example, Er_2O_3 nanospheres were directly decorated on reduced GO sheets to form an Er_2O_3@RGO nanocomposite (in that case for a nitrite sensor) [17]. The fact that Er_2O_3 nanoparticles can be strongly anchored on RGO shows the feasibility of creating Er_2O_3 - GO photocatalysts [18]. Therefore, GO contributes to photocatalysis by (1) providing high surface area and adsorption sites, (2) accepting/transferring electrons to lower recombination, and (3) serving as a structural scaffold. These effects enhance the visible light response and stability of Bi_2O_3 and Er_2O_3 containing composites.

Multicomponent nanocomposites have become a dominant strategy for degrading antibiotics. he combination of Bi_2O_3, Er_2O_3, and GO has not been reported for MNZ specifically, but analogous systems demonstrate the concept. As noted, Bi_2O_3 semiconductor (e.g. $Zn_3In_2S_6$/Bi_2O_3) composites show S-scheme charge separation and greatly accelerated MNZ degradation [19]. Bismuth-based oxyhalides (BiOBr, BiOI) and bismuth vanadate ($BiVO_4$) have been used for other drugs and dyes under visible light [20]. Likewise, GO-supported doped oxides (such as GO–N–ZnO) have achieved near-total MNZ removal [21]. Rare-earth-doped Bi_2O_3 (e.g. Er/Yb co-doping) has given full dye decolorization. Even beyond MNZ, visible-light photocatalysis of similar pharmaceuticals (tetracyclines, ibuprofen, etc.) has been reported with Bi_2O_3-based composites, suggesting broad applicability.

Taken together, the literature shows that Bi_2O_3 supplies visible-light absorption and holes, Er_2O_3 provides up conversion and trap levels, and GO offers rapid electron transfer. For example, a CuO/Bi_2O_3 composite greatly outperformed its components (95.6 % vs 80.5 % / 40.2 % degradation in a dye test). By analogy, a Bi_2O_3 - Er_2O_3 - GO ternary could synergistically combine these advantages. In such a nanocomposite, Bi_2O_3 could absorb visible photons and generate reactive holes, Er_2O_3 could harvest longer-wavelength light (via up conversion) and introduce charge-separated levels, and GO would channel electrons away to oxygen. This architecture is expected to improve light utilization and charge dynamics far beyond any single material.

Despite these promising attributes, a clear understanding of how up conversion-assisted energy transfer, visible-light absorption, and interfacial electron transport can be simultaneously optimized within a single photocatalytic system remains limited. In particular, most reported studies focus on binary composites, while the mechanistic role of rare-earth oxides in multi-component systems for antibiotic degradation under visible light has not been systematically elucidated.

In this work, a ternary Bi_2O_3–Er_2O_3/graphene oxide (GO) nanocomposite is rationally designed to integrate three complementary functionalities: (i) visible-light absorption and hole generation from Bi_2O_3, (ii) upconversion-assisted photon utilization and charge trapping via Er^{3+} centers, and (iii) rapid electron transport through the conductive GO network. Unlike conventional approaches that consider these components independently, this study demonstrates their synergistic coupling and identifies an optimal composition that maximizes photocatalytic performance. By correlating structural, optical, and photophysical properties with degradation efficiency, this work provides mechanistic insight into charge separation and transfer pathways in ternary photocatalysts. To the best of our knowledge, this is the first systematic investigation of Bi_2O_3–Er_2O_3/GO nanocomposites for visible-light-driven metronidazole degradation, offering a framework for the rational design of advanced photocatalysts for emerging pharmaceutical contaminants.

2. Materials and Method

2.1. Chemicals

All chemicals used in this study were of analytical grade and utilized without further purification. Bismuth nitrate pentahydrate ($Bi(NO_3)_3 \cdot 5H_2O$) and erbium nitrate pentahydrate ($Er(NO_3)_3 \cdot 5H_2O$) were obtained from Macklin (China). Graphite powder, used as the precursor for graphene oxide synthesis, was supplied by Glentham Life Sciences (UK). Sodium hydroxide (NaOH, 99%) and ethanol (C_2H_5OH, 99%) were purchased from Alpha Chemika (India). Nitric acid (HNO_3, 65%) was obtained from Riedel-de Haën (Germany). Metronidazole ($C_6H_9N_3O_3$), the

model pollutant, was also procured from Macklin (China). All aqueous solutions were prepared using freshly distilled water.

2.2. Synthesis of Graphene Oxide

GO was synthesized via the modified Hummers' method [22]. Briefly, graphite powder was oxidized using $KMnO_4$ in a mixture of H_2SO_4 and H_3PO_4, followed by washing, centrifugation, and drying at 60 °C.

2.3. Preparation of Bi_2O_3 Doped Er_2O_3/GO Nanoparticles

To synthesize 2 grams as selected amount of Bi_2O_3 doped Er_2O_3/GO nanocomposite, a co-precipitation method was employed. Initially, 1.0 g of graphene oxide (GO), previously prepared via the modified Hummers' method, was dispersed in 100 mL of deionized (DI) water under ultrasonication for 1 hour to ensure complete exfoliation and homogeneous dispersion. Separately, stoichiometric amounts of bismuth nitrate pentahydrate ($Bi(NO_3)_3 \cdot 5H_2O$) and erbium nitrate pentahydrate ($Er(NO_3)_3 \cdot 5H_2O$) were accurately weighed to obtain a Bi:Er molar ratio of 4:1, suitable for co-doping, and a total metal loading corresponding to the remaining 1.0 g of target composite mass (accounting for GO content). Specifically, 1.32 g of $Bi(NO_3)_3 \cdot 5H_2O$ was dissolved in suitable amount of HNO_3 then add to 50 mL of DI water because Bismuth nitrate not dissolved in water directly and 0.23 g of $Er(NO_3)_3 \cdot 5H_2O$ were dissolved in 50 mL of DI water under stirring to form a clear solution.

The metal nitrate solution was then slowly added dropwise to the GO suspension under continuous magnetic stirring at room temperature. Once fully added, the pH of the mixture was adjusted to ~10 using 0.3 M NaOH solution added dropwise very slowly under vigorous stirring using burette to insure no particles agglomeration, inducing co-precipitation of metal hydroxides onto the GO sheets. The resulting suspension was stirred vigorously for 4 hours at 65 °C to facilitate nucleation and growth of BiEr nanoparticles on the GO surface. The product was then aged at room temperature for 24 hours to improve crystallinity.

After aging, the precipitate was separated by centrifugation at 4000 rpm for 10 minutes, washed three times with DI water and twice with ethanol to remove residual ions and impurities. The solid was then dried in a vacuum oven at 80 °C for 24 hours. Finally, the dried powder was calcined at 350 °C for 2 hours in a muffle furnace to improve crystallinity and stability. The result was a fine gray-black powder. The above procedure was repeated for the remaining samples. It was configured depending on the percentage of GO. The GO percentages involved were 0% GO (M1), 20% GO (M2), and 40% GO (M3).

2.4. Characterizations of Zinc Oxide Nanoparticles

The structural, morphological, compositional, and optical properties of the synthesized BiEr/GO nanocomposite were systematically characterized using a range of analytical techniques. X-ray diffraction (XRD) analysis was performed using a Bruker D8 Advance diffractometer with Cu-Kα radiation (λ = 1.5406 Å) over a 2θ range of 10°-80°. The surface morphology and particle distribution were examined using scanning electron microscopy (SEM) (FEI Quanta 450). That revealed a rough, layered GO surface uniformly decorated with spherical BiEr nanoparticles. To gain further insight into the nanostructure, transmission electron microscopy (TEM) (JEOL JEM-2100) was employed. It showed well-dispersed crystalline nanoparticles anchored on the GO sheets with particle sizes ranging between 15-30 nm. Energy-dispersive X-ray spectroscopy (EDX) coupled with SEM confirmed the elemental composition and homogeneous distribution of Bi, Er, C, and O within the composite. Fourier-transform infrared spectroscopy (FTIR) (Thermo Nicolet iS10) was used to identify functional groups and bonding interactions. The optical properties were evaluated using UV-Vis diffuse reflectance spectroscopy (UV-Vis DRS) (Shimadzu UV-2600). The BiEr/GO composite showed strong absorption in the visible light region. It also showed a redshift compared to pristine GO. The photoluminescence (PL) spectroscopy (Horiba Fluorolog-3) was conducted to investigate the recombination behavior of photo-generated charge carriers.

2.5. Photocatalytic Reaction Testing

An aqueous solution of metronidazole with an initial concentration of 100 mg/L was prepared. The preparation proposed by dissolving the appropriate mass of the compound in 100 mL of deionized water. The photocatalyst was introduced into this solution at a dosage of 0.1 to 0.5 g/L. The pH varied from 2 to 10, and the resulting suspension was magnetically stirred in the dark for 30 min. The purpose of was to establish adsorption-desorption equilibrium between the pollutant molecules and the catalyst surface. After equilibration, the reactor was exposed to visible light from a 300 W Xenon lamp. The lamp was positioned at the fixed distance about 20 cm from the surface of the solution to ensure uniform illumination. Continuous stirring was used to prevent particle sedimentation and ensure homogeneous exposure. The

photocatalytic reaction was carried out for 190 min. During this period, 5 mL samples were withdrawn at 20 min intervals. Each sample was immediately centrifuged to remove suspended catalyst particles. The floating material was analyzed with UV to quantify the residual metronidazole concentration. Control experiments, including adsorption in the dark, photolysis in the absence of catalyst, were performed under identical conditions. That was done for the purpose of discriminating between direct photolysis, adsorption, and true photocatalytic activity. All experiments were conducted twice, and Figure 1 shows the experimental setup. The reported data are mean values with the associated standard deviations. That was planned to ensure reproducibility and statistical reliability.

For recyclability assessments, best photocatalyst sample was terminated at 190 min. Then, the catalyst was recovered by centrifugation (6000 rpm, 10 min). Then it was washed thoroughly with deionized water three times and ethanol once to remove adsorbed residues. Then, it is dried at 60 °C for 12 h. The dried powder was then re-dispersed into fresh 100 mg/L metronidazole solution at the same dosage (0.3 g/L). Evaluating the resulting solution occurred under the same exposure and sampling conditions for five consecutive cycles.

3. Results and Discussion

3.1. FTIR Characterization

Figure 2 shows the FTIR spectrum of M1. In there, the characteristic vibrational features of with metal-oxygen bonds and surface functional groups appear. Strong absorption bands are observed in the low-wavenumber region (below ~700 cm^{-1}). They are due to Er-O and Bi-O stretching vibrations. This proves the formation of the metal oxide framework. A broad band around ~3400 cm^{-1} and a weaker band near ~1600–1650 cm^{-1} also appear. Ther are due to O-H stretching and bending vibrations, respectively. Those are caused by surface-adsorbed water or hydroxyl groups commonly found on oxide materials. These surface

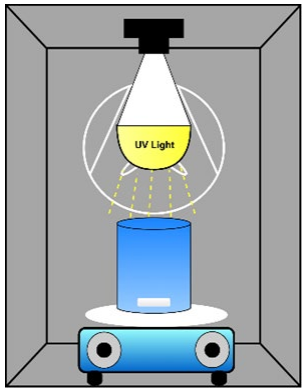

Figure 1. Experimental setup.

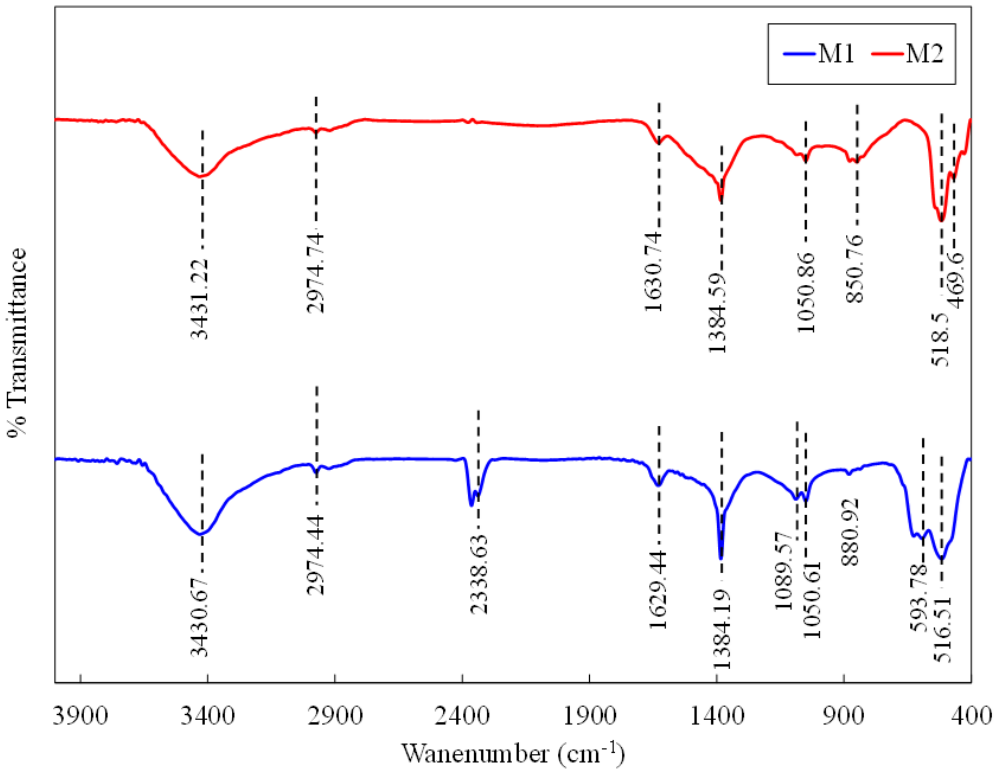

Figure 2. The FTIR for M1 and M2.

hydroxyls are important since they act as active sites in catalytic reactions. In the FTIR spectrum of M2, the metal-oxygen vibration bands remain present in the low-wavenumber region. This shows that the fundamental oxide structure is conserved after introducing graphene oxide. This observation is in agreement with the XRD results. Those results showed no phase transformation when GO was added. However, obvious differences appear in the mid- and high-wavenumber regions compared to M1. Specifically, M2 shows additional absorption bands special to graphene oxide functional groups. These typically include bands associated with C=O stretching (around ~1700–1730 cm^{-1}), C=C skeletal vibrations of sp^2 carbon (around ~1580–1620 cm^{-1}), C–O–C (epoxy) stretching (~1200–1250 cm^{-1}), and C–O (alkoxy) stretching (~1050–1100 cm^{-1}). The broad O-H stretching band around ~3400 cm^{-1} in M2 is generally more intense than in M1. This indicates the higher density of hydroxyl and oxygen-containing groups introduced by graphene oxide.

3.2. X-Ray Diffraction

Figure 3 shows the XRD patterns of M1 and M2. They show sharp and well-defined diffraction peaks. This indicates that the crystalline nature of the metal oxide phase remains in both samples. In both cases, the dominant reflections are due to cubic Er_2O_3. The most intense peak appears at around $2\theta \approx 29–30°$, in both cases. Additional distinguishing peaks appear at higher angles. This proves that Er_2O_3 remains the primary crystalline phase in spite of graphene oxide incorporation. A comparison of the two patterns shows that the peak positions in M2 are very close to those of M1. This shows that the addition of graphene oxide does not cause any phase transformation or structural change in the Bi_2O_3-doped Er_2O_3 lattice. Additional diffraction peaks in M2 are missing. This reinforces the statement that no new crystalline impurity phases are formed when GO was added. This proves that the oxide catalyst and the carbon-based support are structurally compatible. Important differences are seen in peak intensity and width between M1 and M2. In M2, many diffraction peaks appear a little broader and less intense compared to M1. This is due to many causes. Among these causes are the reduced crystallite size and the increased lattice strain. The strong interfacial interactions between the oxide particles and graphene oxide sheets could also be a factor. These effects are frequently observed in oxide-carbon composites. They indicate improved dispersion of the active oxide phase on the GO surface. Additionally, no distinct diffraction peak due to graphene oxide (typically near $2\theta \approx 10–12°$) is seen in the M2 pattern. This suggests that the graphene oxide is either highly exfoliated or present in an amorphous or poorly ordered form. Being exfoliated or amorphous cause weak or undetectable diffraction signals.

3.3. BET Surface Area

The nitrogen adsorption-desorption isotherm of M1 (Figure 4a) exhibits a typical type IV isotherm with a hysteresis loop. This is a distinguishing feature of mesoporous materials. Gradual increase in adsorption, and monolayer adsorption on the external surface of the oxide

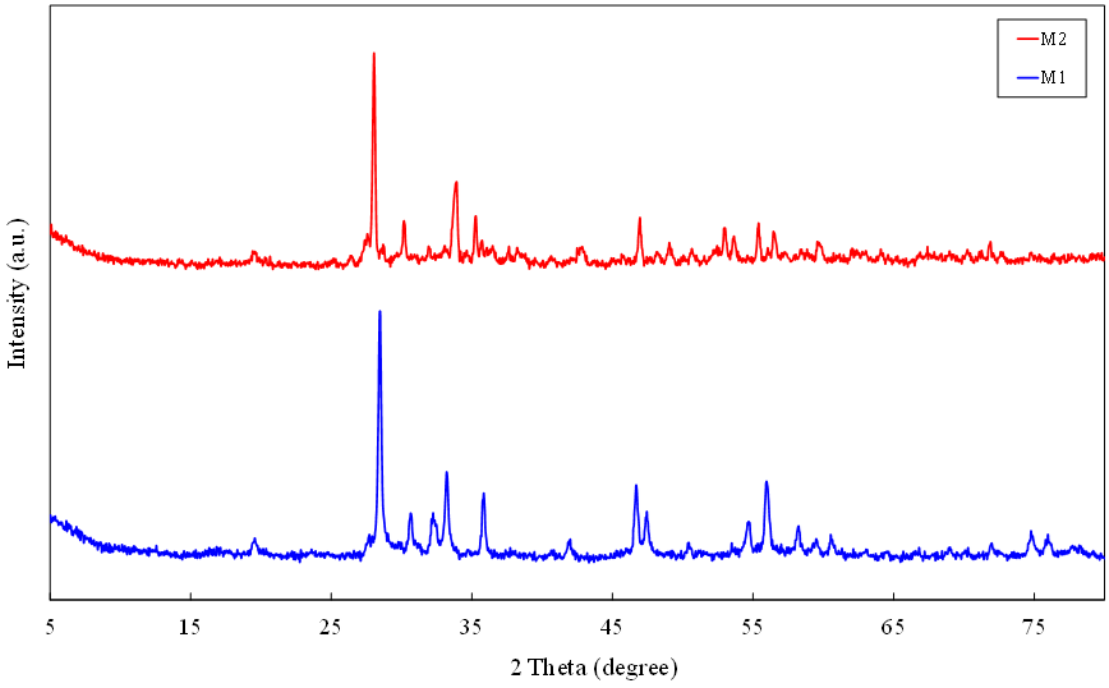

Figure 3. The XRD pattern for the M1 and M2.

particles are seen. Those two conditions at low relative pressures (p/p_0 < 0.1) indicates limited microporosity. A rapid rise in nitrogen uptake is observed at high p/p_0 values (≈ 0.8-1.0). This is seen when the relative pressure increases. That is caused by capillary condensation within mesopores. A well-defined hysteresis loop between the adsorption and desorption branches is seen. That shows the mesoporous nature of M1. This loop is probably formed from interparticle voids and agglomeration of oxide crystallites. Figure 4b shows the isotherm of M2. There is a type IV profile with hysteresis. This indicates that the mesoporous structure remains after graphene oxide incorporation. The overall nitrogen uptake of M2 is significantly different from that of M1. That is especially so in the high relative pressure region. The reduced adsorption volume at p/p_0 ≈ 1.0 suggests changes in pore volume and pore accessibility. This is due to including of graphene oxide sheets within the oxide matrix. Table 1 shows the pore volume and mean pore diameter for M1 and M2 samples.

3.4. Photoluminescence (PL) Analysis

Photoluminescence (PL) spectroscopy was used to examine recombination of photogenerated charge carriers in Bi_2O_3-Er_2O_3/GO nanocomposites. Figure 5 compares the PL spectra of M1 (0% GO), M2 (20% GO), and M3 (40% GO). The GO-free sample (M1) shows the highest emission intensity. This shows that a high probability of radiative recombination is met in the original oxide matrix. This is mostly seen for metal-oxide semiconductors in which defect-assisted recombination centers are dense [23, 24]. After incorporating GO (M2 and M3), a clear PL quenching is observed. That proves the effect of GO as an electron acceptor/transport platform. This enables interfacial charge transfer and suppresses electron-hole recombination [25-27]. M2 (20% GO) displays the strongest quenching in most of the studied range. This shows that moderate GO loading provides an optimal interfacial contact enabling efficient electron extraction. At the same time sufficient photon absorption by the semiconductor phase is maintained [25]. In contrast, M3 (40% GO) shows higher emission than M2 in the long-wavelength region. This might be due to excess GO. That causes partial shielding of the active oxide surface. Further, aggregation, or the formation of additional interfacial defect states that contribute to radiative transitions proceeds. This was reported in carbon-assisted semiconductor composites at high carbon content [26, 27]. The PL results indicate that incorporation of GO largely improves charge separation. All is compared with the GO-free sample, with the most effective recombination suppression achieved for the 20% GO composite (M1). That is expected to enable improved photocatalytic performance [25].

Table 1. Pore volume and mean pore diameter for M1 and M2.

Sample	Pore volume (cm^3/g)	Mean pore diameter (nm)
M1	0.074317	30.249
M2	0.052397	27.27

3.5. UV–Vis Diffuse Reflectance Spectroscopy (DRS)

Figure 6 presents the diffuse reflectance spectra of M1 (0% GO), M2 (20% GO), and M3 (40% GO) over the wavelength range of 200-1000 nm. The pristine Bi_2O_3-Er_2O_3 sample (M1) shows relatively high reflectance in the ultraviolet and

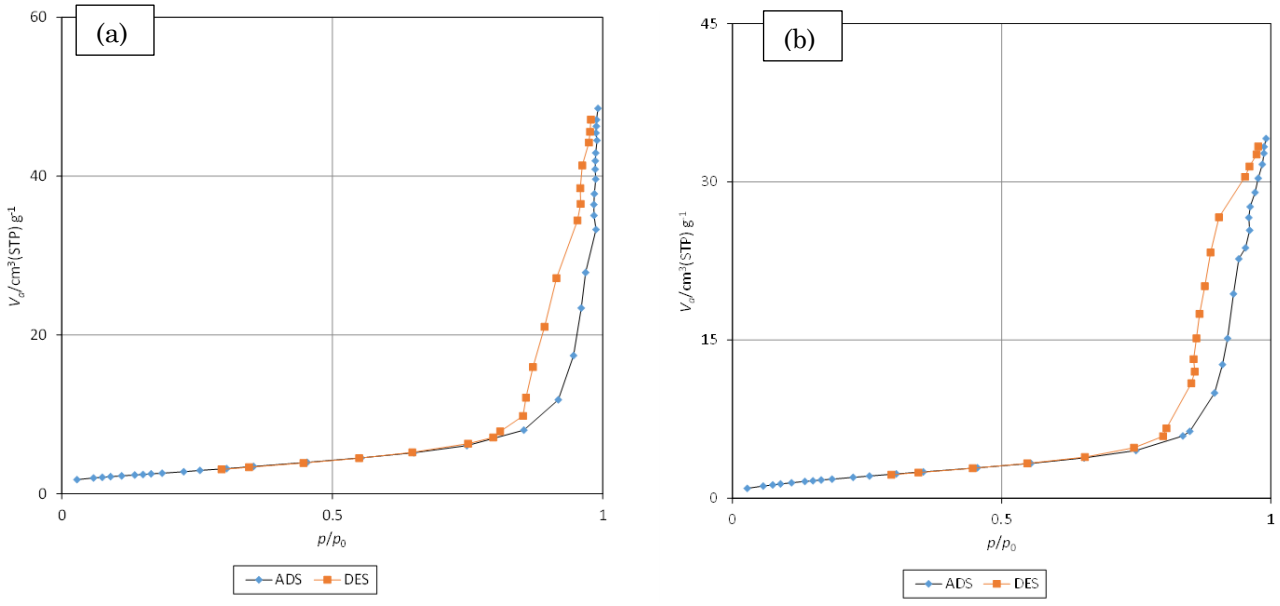

Figure 4. BET adsorption-desorption isotherm for M1 (a) and M2 (b).

visible regions. That indicates limited light absorption and a wide optical band gap. This is a distinguishing feature of metal oxide semiconductors with weak visible-light utilization. When graphene oxide is incorporated, a significant reduction in reflectance intensity is observed for both GO-containing samples. This proves improved photon absorption due to strong interfacial electronic coupling between GO and the Bi_2O_3-Er_2O_3 matrix [28]. The presence of GO introduces additional electronic states and eases interfacial charge-transfer transitions. This way, light absorption is extended into the visible region [29]. Among the composites, M2 (20% GO) shows the lowest reflectance over a wide wavelength range. This indicates the most efficient light-harvesting capability. In contrast, M3 (40% GO) shows slightly higher reflectance than M1. This shows that excessive GO loading leads to partial surface shielding or aggregation effects. Those effects limit effective photon penetration into the active semiconductor phase. The optical band-gap energies were estimated using the Kubelka-Munk function and Tauc plots. Both direct allowed and indirect allowed electronic transitions were considered. That was to make sure the interpretation is robust. This is commonly adopted for Bi_2O_3-based composite systems [30]. A clear red shift of the absorption edge is seen in M2 (20% GO) toward longer wavelengths (~516 nm) compared with M1 (0% GO) (~436 nm) and M3 (40% GO) (~433 nm). That indicates significant band-gap narrowing was caused by optimal GO incorporation. From the Tauc analysis, the direct band-gap energy of M1 is estimated to be approximately 2.84 eV. Incorporating 20% GO

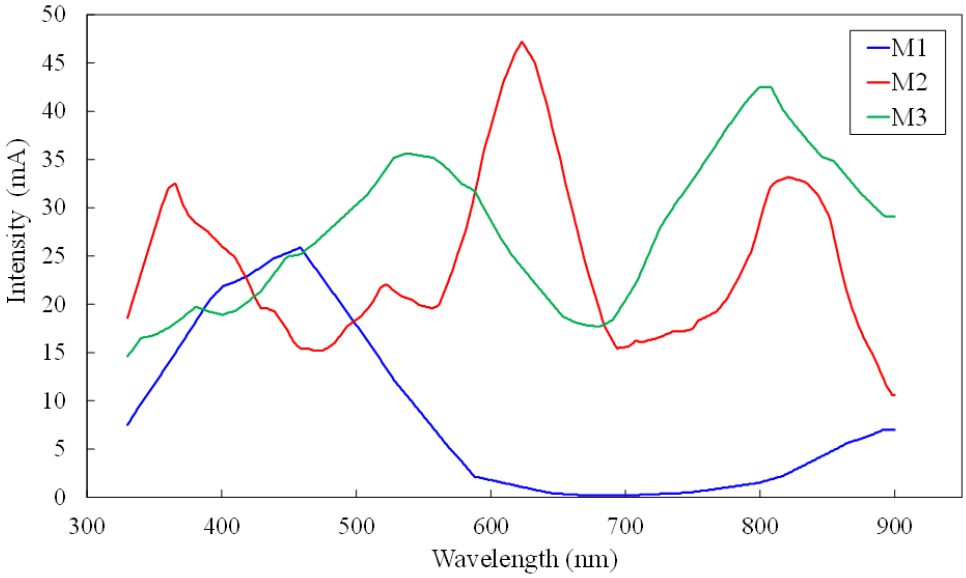

Figure 5. PL spectroscopy analysis for M1, M2, and M3.

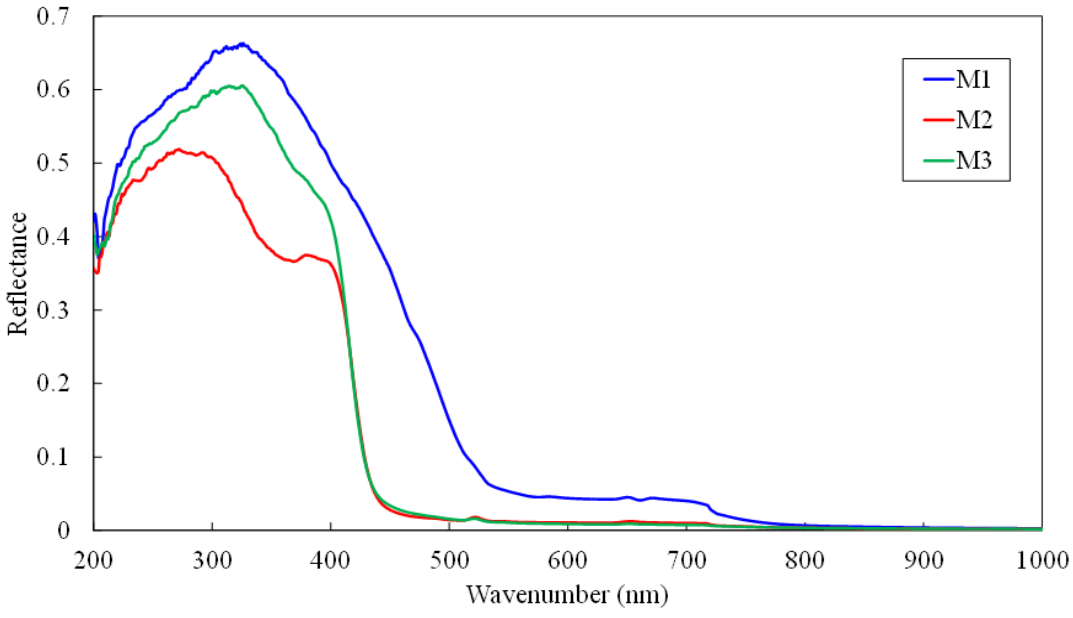

Figure 6. UV–Vis Diffuse Reflectance Spectroscopy (DRS) analysis.

reduces the band gap to approximately 2.40 eV. This showed improved visible-light response. However, increasing GO content to 40% results in a band gap (~2.86 eV) comparable to that of the GO-free sample. This shows saturation of interfacial electronic effects at higher GO loading. The observed band-gap narrowing at moderate GO content can be attributed to electronic coupling between Bi_2O_3-Er_2O_3 and GO. Additional contributions were from the formation of interfacial charge-transfer states. Defect-mediated sub-band-gap levels are also thought to contribute. Extreme GO loading, however, does not further improve optical absorption and may instead introduce light-screening effects. That have a counteracting effect due to band-gap modulation. These DRS results are in full agreement with with PL analysis. There, M1 (20% GO) showed the strongest suppression of radiative recombination. Thus, improved charge separation efficiency is proved. In general, the combined optical analyses demonstrate that 20% GO provides the most effective balance between improved light absorption and efficient charge-carrier dynamics. That is expected to result in superior photocatalytic performance [30].

3.6. Transmission Electron Microscopy (TEM) Analysis

Figure 7a and Figure 7b show TEM images of the composites containing 20% GO and 40% GO. Those images were taken at high magnification with a scale bar of 75 nm. TEM analysis provides complementary nanoscale structural information that cannot be fully resolved by FESEM. That is especially true for particle size distribution and oxide-GO interfacial contact [31].

For the 20% GO composite, the TEM image shows a uniform spread of nanosized Bi_2O_3-Er_2O_3 particles attached to a relatively thin and partially transparent GO matrix. The oxide nanoparticles appear almost spherical and form interconnected clusters with nanoscale dimensions. There was clear separation between those particles and no severe accumulation. The semi-transparent background regions correspond to GO sheets. That indicates close contact between the metal oxide nanoparticles and the GO support. This configuration makes interfacial charge transfer highly efficient. That is because electrons generated within the oxide phase can be efficiently transported to the conductive GO network. Thus, electron-hole recombination is suppressed [32].

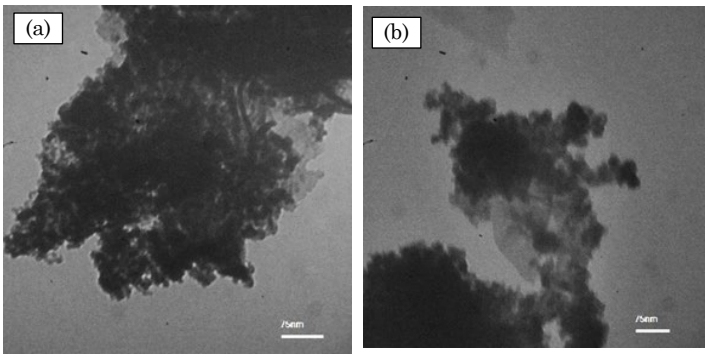

Figure 7. TEM analysis for M2 (a) and M3 (b).

The TEM image of the 40% GO composite shows a significantly different structural arrangement. Although Bi_2O_3-Er_2O_3 nanoparticles are still present, the GO sheets appear thicker and more overlapped, indicating partial restacking due to excessive GO content. The oxide particles are embedded within denser carbon-rich regions, and localized aggregation can be observed. This structural feature suggests reduced accessibility of the active oxide surface and increased diffusion resistance for charge carriers, which may hinder effective interfacial charge separation despite the higher GO loading [33]. The TEM observations are in excellent agreement with FESEM results, where the 20% GO composite exhibited uniform nanoparticle distribution and porous surface architecture, while the 40% GO sample showed signs of structural compaction and aggregation. Furthermore, the TEM-derived interfacial structure strongly correlates with optical analyses: the optimized dispersion and intimate oxide–GO contact in the 20% GO composite explain the strong PL quenching (reduced radiative recombination) and band-gap narrowing observed in DRS, whereas the restacked GO structure in the 40% GO sample is consistent with reduced optical benefits due to shielding and saturation effects.

The TEM results confirm that moderate GO incorporation (20%) yields an optimal nanoscale architecture, characterized by well-dispersed oxide nanoparticles and efficient interfacial coupling with GO sheets. Excessive GO loading (40%) leads to restacking and partial encapsulation of the oxide phase, which diminishes the structural and electronic advantages. These findings provide direct nanoscale evidence supporting the PL and DRS results and explain the superior photocatalytic behavior expected for the 20% GO composite.

3.7. Scanning Electron Microscopy (SEM) Analysis

Figure 8 presents a representative high-magnification FESEM image of sample A (20% GO) recorded at 250,000× with a scale bar of 300 nm. FESEM analysis is particularly useful for evaluating particle dispersion, surface texture, and interfacial contact in graphene-based composite photocatalysts, which strongly

influence charge transfer and catalytic behavior [34].

As observed in Figure 8, the surface of sample A is composed of densely packed, quasi-spherical nanoparticles forming a highly rough and porous nanostructure. The nanoparticles are uniformly distributed and closely interconnected, creating a continuous network with abundant grain boundaries. Such nanoscale particle assemblies are advantageous for photocatalytic applications. They provide a large number of active sites and facilitate efficient diffusion of reactants and products. At this degree of magnification, individual GO sheets are not distinguished as isolated planar layers. However, the wrinkled background texture and homogeneous anchoring of oxide nanoparticles show their presence. This is a commonly seen feature in metal-oxide/GO composites. The close contact between Bi_2O_3-Er_2O_3 nanoparticles and the GO substrate indicates strong interfacial interaction. That is important for rapid electron transport from the semiconductor to the conductive GO network. In this way charge carrier recombination is blocked [35].

No large agglomerates or isolated oxide clusters are seen in sample A. This suggests that 20% GO effectively prevents excessive particle aggregation during synthesis. The formation of nanoscale voids between interconnected particles results in a porous structure. That improves light penetration and mass transfer and maintains enough exposure of active oxide sites. This advantageous morphology explains an important observation. It is consistent with the strong PL quenching and improved visible-light absorption seen for the 20% GO composite. That shows improved charge separation and light-harvesting efficiency. The FESEM results show that 20% GO leads to a well-dispersed nanoparticle network. This network is of high surface roughness and strong interfacial coupling. That provides a structurally optimized platform for photocatalytic reactions. The morphological features observed here support the optical analyses (PL and DRS). It strengthens the conclusion that moderate GO incorporation offers a most effective balance. This level balances structural integrity, electronic interaction, and catalytic performance.

3.8. Effect of Initial Concentration

Figure 9 contains a detailed visualization of the effect of initial pollutant concentration on the efficiency of the photocatalytic degradation. The initial part of the graph (0 to 30 minutes) represents the dark adsorption phase. During this time, the concentration remains relatively constant for all samples. This shows adsorption of metronidazole onto the catalyst surface is minimal. The main action begins after 30 minutes. That is when the UV light source on. The inverse relationship between initial concentration is significantly observed under UV light. The 50-ppm sample shows the sharpest decline in reaching near-total degradation. The degradation in that case happened within 180 minutes. The efficiency decreases as the initial concentration increases (75 ppm, 100 ppm, and 125 ppm). The 125-ppm sample showed the slowest rate of degradation. In that sample, approximately 20%

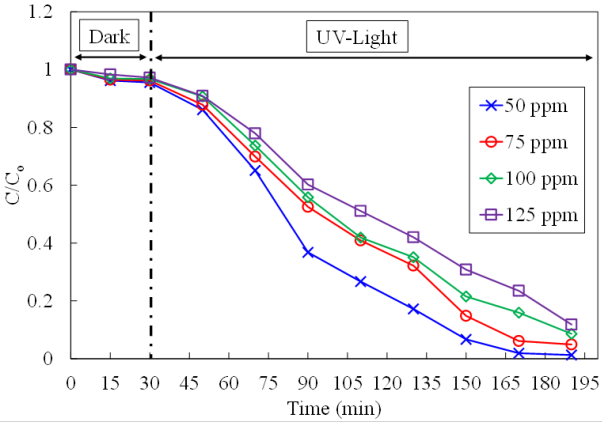

Figure 9. The effect of the concentration of metronidazole at pH of 8 using 0.3 g of M2.

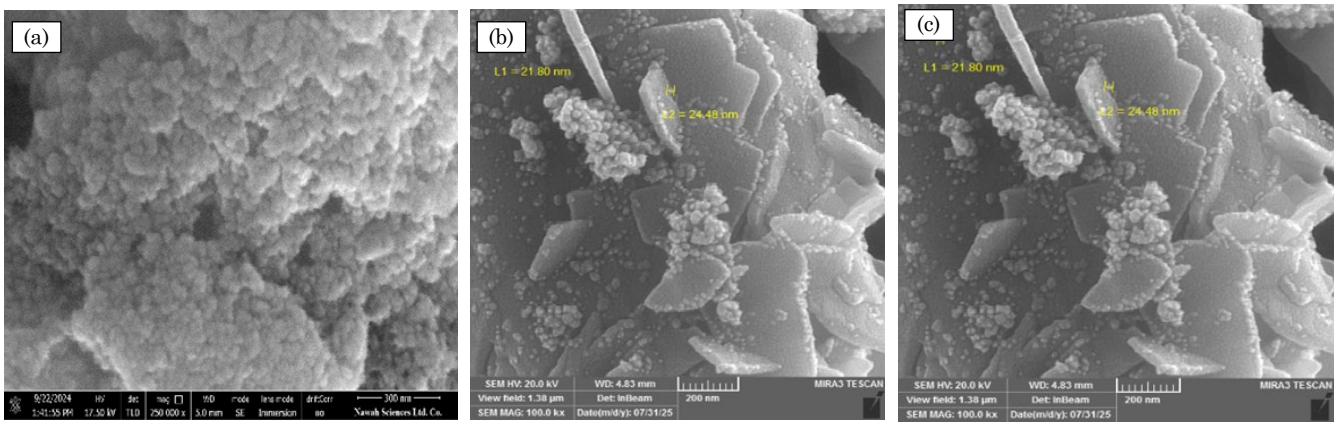

Figure 8. SEM analysis for M1 (a), M2 (b), and M3 (c).

of the original metronidazole remained after 195 minutes. This difference in performance is due to the limited number of active sites and reactive species. As the concentration of metronidazole increases, the capacity of a fixed amount of catalyst is exceeded. That leads to saturating the active sites. Besides, the higher pollutant concentration causes a "filter effect,". That is where metronidazole molecules block UV light from reaching the catalyst surface effectively. That would prevent generating the necessary radicals for efficient degradation.

The decrease in degradation efficiency at higher initial MDZ concentrations can be explained by both kinetic limitations and photocatalyst properties. Although the Bi_2O_3-Er_2O_3/GO composite exhibits enhanced light absorption and reduced charge recombination, as confirmed by DRS and PL analyses, the excessive pollutant concentration limits photon penetration and active site availability. Consequently, the generation of reactive species becomes insufficient relative to the pollutant load. Nevertheless, the superior performance at lower concentrations highlights the effectiveness of the composite's charge transfer characteristics and its ability to sustain reactive radical formation under optimized conditions.

3.9. Effect of Percentage of GO

Figure 10 shows the effect of varying the weight percentage of graphene oxide (GO) on the photocatalytic degradation efficiency of metronidazole under UV light. The figure clearly shows that the inclusion of GO significantly improves the catalytic activity of the system. M2 showed the most effective degradation compared to the catalyst (M1) and the catalyst with excess GO (M3). The improved performance of sample M2 is due to improved charge separation within the composite material. Graphene oxide acts as an efficient electron acceptor and transporter. Therefore, the photo-generated electrons are drawn away from the semiconductor component of the catalyst. This mechanism significantly prevents the rapid recombination of electron-hole pairs. Therefore, more charge carriers are allowed to migrate to the catalyst surface. The charge carriers can generate the reactive oxygen species needed to degrade the metronidazole molecules. The high surface area of GO also contributes by potentially increasing the adsorption capacity for the pollutant near the active sites. The charge transfer mechanism seems the largest contributor. The observed trend also points out the importance of finding an optimal GO loading. The 0% GO sample (M1) is the the worst case because of high electron-hole recombination. The 40% GO sample (M3) is worse than the 20% GO sample (M2). This shows that excessive GO can have negative impact. A high concentration of GO might begin to block the catalyst's active sites. It might also impede the penetration of UV light into the solution (an inner filtration effect). That reduces the amount of light reaching the semiconductor and thus slows down the overall degradation process. The 20% GO concentration represents the ideal balance for optimal performance in this specific reaction system.

3.10. Effect of Catalyst Dose

Figure 11 shows the effect of varying the catalyst dose (from 0.1 g to 0.5 g) on the photocatalytic degradation efficiency of metronidazole. The experimental setup include a pH of 8 and a catalyst composition featuring 20% graphene oxide. During the first 30-minute dark period, the concentration of MNZ remains stable for all catalyst doses. This indicates that physical adsorption of the pollutant onto the catalyst surface is negligible before light activation. When UV light is on, degradation begins in all samples, but the rates vary significantly. The lowest dose of 0.1 g shows the slowest degradation. In that

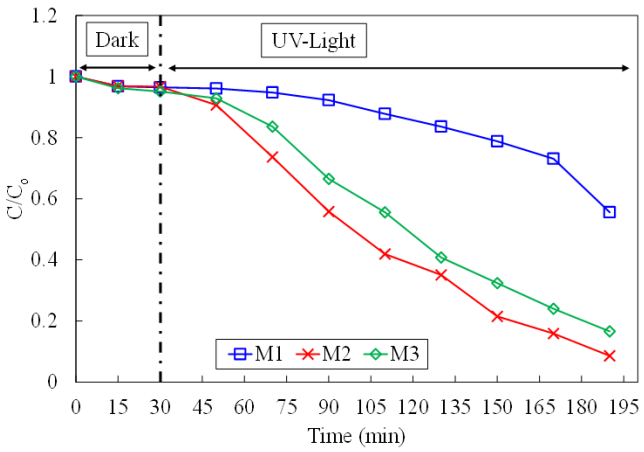

Figure 10. The effect of the percentage of graphene oxide on the photodegradation of 100 ppm of metronidazole at pH of 8.

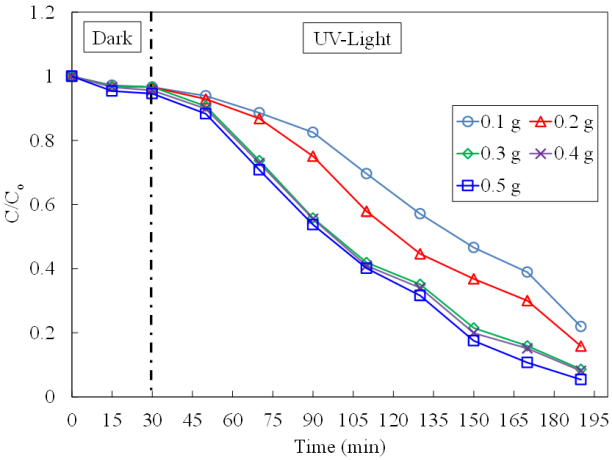

Figure 11. The effect of the M2 photocatalyst dose on the photodegradation of 100 ppm of metronidazole at pH of 8.

sample, the highest amount of residual MNZ resulted in 195 minutes. The efficiency improves noticeably with 0.2 g and increases more with 0.3 g, 0.4 g, and 0.5 g of catalyst mass.

The main reason for this improved efficiency with increasing catalyst mass is the direct increase in the total number of active sites available for the reaction. A higher catalyst dose provides more surface area. That higher area permit MNZ molecules to adsorb more and interact with the light-generated reactive oxygen species (like hydroxyl radicals). This scenario happens at the optimal pH of 8. This causes better utilization of the incident light and faster degradation. However, at doses of 0.3 g, 0.4 g, and 0.5 g the degradation begins to plateau. The degradation curves for these masses are almost identical. This indicates that a saturation point is reached where adding more catalyst no longer improves the reaction rate. At this saturation limit the amount of available UV light becomes the new limiting factor due to the inner filtration effect.

The observed dependence of degradation efficiency on catalyst loading can be directly correlated with the physicochemical properties of the Bi_2O_3-Er_2O_3/GO composite. At optimal loading, the enhanced performance is attributed to efficient charge separation, as evidenced by the reduced photoluminescence (PL) intensity, indicating suppressed electron–hole recombination. Additionally, diffuse reflectance spectroscopy (DRS) results demonstrate improved visible-light absorption due to bandgap narrowing, allowing greater photon utilization. The presence of GO further facilitates electron transport, promoting the formation of reactive oxygen species. At higher catalyst dosages, however, light scattering and reduced penetration limit photoactivation, thereby decreasing overall efficiency despite favorable material properties.

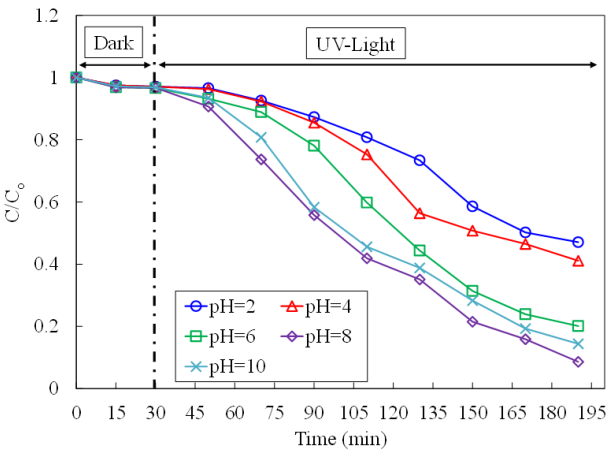

Figure 12. The effect of pH on the photodegradation of 100 ppm of metronidazole using 0.3 g of M2.

3.11. Effect of pH

Figure 12 compares the effectiveness of metronidazole photodegradation for many initial pH values. The first half-hour of the experiment shows a flat line for all data sets. In all of the experiments, this first half-hour is designated as the pre-exposure or "dark" phase. This indicates that adsorption is not a significant removal mechanism in this system. That is so since the pollutant concentration does not drop until the catalyst is exposed to UV light. Once the UV light is introduced after the first 30-minute, a clear degradation trend begins. The efficiency is largely dependent on the solution's alkalinity. The data shows a strong positive correlation between pH values and degradation rate. The experiments conducted for pH values of 10 and 8 show the most rapid decrease in metronidazole concentration. Those achieved the highest removal rates. Conversely, the acidic conditions (pH 2 and pH 4) result in significantly slower degradation. The pH 2 data show the slowest reduction in concentration during the 195-minute period. This suggests that the generation of primary reactive oxygen species, such as hydroxyl radicals, is highly favored in alkaline environments. Further, the stability of those species is also favored by alkaline environments. Therefore, the catalyst becomes far more efficient in basic than in acidic solutions.

The influence of pH on photocatalytic performance is not only related to surface charge interactions but also reflects the intrinsic charge transfer properties of the composite. The improved degradation efficiency under optimal pH conditions is consistent with the enhanced charge separation behavior observed in PL analysis and the effective visible-light absorption indicated by DRS measurements. Furthermore, the well-integrated interface between Bi_2O_3, Er_2O_3, and GO, as observed in morphological characterization, supports efficient electron migration across the heterostructure. These properties collectively facilitate the generation of reactive radical species, thereby enhancing degradation efficiency under favorable pH conditions.

3.12. Reusability, Stability, and Recyclability

The long-term stability and recyclability of a photocatalyst are critical factors for its practical application in wastewater treatment systems. Therefore, the photocatalytic durability of the Bi_2O_3-Er_2O_3/20%GO (M2) composite was evaluated for five successive degradation cycles of metronidazole. After each run, the M2 catalyst was separated using ultracentrifugation. The catalyst was then washed with deionized water. Lastly, it was dried at 80 °C to remove any intermediates. Figure 13 shows that the

photocatalytic activity decreased only slightly after the fifth cycle. The overall reduction was approximately 15.2%. This minor decay can be attributed to partial catalyst deactivation. Surface fouling by degradation intermediates was also a factor. Material loss during recovery also contributed. The catalyst kept a high removal efficiency. That showed excellent structural integrity and reusability.

XRD analysis was conducted after the fifth reuse cycle, as shown Figure 14. That was to prove the structural stability of the recycled photocatalyst more. The diffraction pattern of the used Bi_2O_3-Er_2O_3/20%GO sample had all the distinguishing peaks of Bi_2O_3 and Er_2O_3 phases. This indicates that no phase transformation or structural collapse occurred during repeated photocatalytic operation. The peaks were seen to be slightly less intense and wide. That might be due to partial loss of crystallinity. Mild accumulation of active metal oxide particles, or surface coverage by residual organic species could be factors. No new impurity peaks appeared. This showed that the catalyst did not experience any undesirable chemical reactions or decomposition during photodegradation. These observations, taken together, show that the Bi_2O_3-Er_2O_3/20%GO nanocomposite maintains good structural stability and photocatalytic performance. This conclusion is not affected by multiple reuse cycles.

3.13. Comparison with Previously Reported Photocatalytic Systems

To evaluate the effectiveness of the developed photocatalyst, a comparative analysis with previously reported systems for metronidazole (MTZ) degradation is presented in Table 2. The comparison includes key operational parameters such as initial pollutant concentration, catalyst dosage, light source, and reaction time. As shown, several reported systems achieve high degradation efficiencies; however, many rely on UV irradiation, higher catalyst dosages, or extended reaction times. In contrast, the present

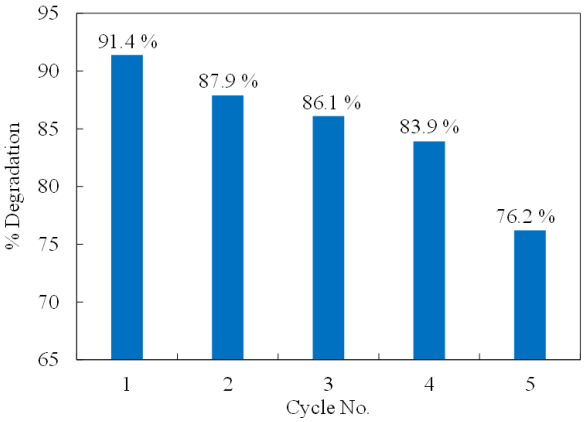

Figure 13. Percentage degradation of M2 with cycle number.

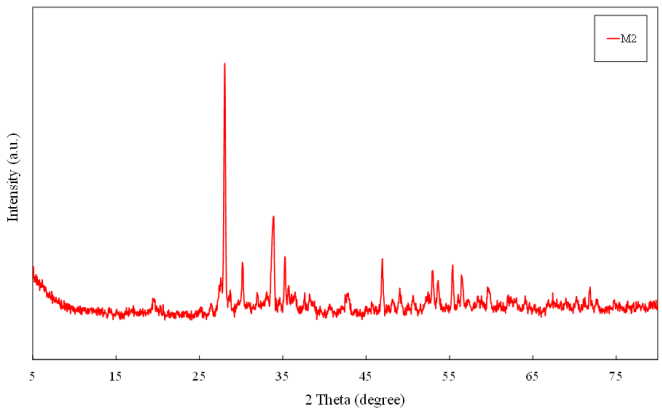

Figure 14. XRD for M2.

Table 2. Comparative evaluation of photocatalytic degradation of metronidazole (MTZ) using various photocatalysts reported in the literature and the present Bi_2O_3-Er_2O_3/GO system.

Photocatalyst	MTZ conc.	Photocatalyst Dose	Light Source	Time (min)	% Degradation	Ref.
Amino acid glycine-modified TiO_2/Fe_3O_4 heterojunction immobilized on chitosan-Polyacrylonitrile	40 mg/L, pH 4.5	0.50 g/L	Visible Light	120	95.7	[36]
TiO_2, P25 (lab & CPC pilot scale)	10 mg/L	0.50 g/L	UV / Solar	60 to 120	100, 91	[37]
ZnO/AC nanocomposite (hydrothermal)	80 mg/L, pH 9	0.90 g/L	UV	300	99	[38]
EG-ZnO NPs (watermelon peel biosynthesis)	170 mg/L, pH 5	0.2061 g/L	UV	10	78.14	[39]
Co/g-C_3N_4/Fe_3O_4 nanocomposite (hydrothermal)	5 mg/L, pH 8	0.70 g/L	Visible Light	60	99	[40]
Fe_3O_4@HZSM-5	25 mg/L, pH 7	0.40 g/L, H_2O_2 1mM	Visible Light	40	98	[41]
Bi_2O_3-Er_2O_3/20%GO	100 mg/L, pH 8	0.50 g/L	UV	190	94.6	Current study

Bi_2O_3–Er_2O_3/GO nanocomposite demonstrates high degradation efficiency under visible light irradiation without the need for additional oxidants, highlighting its potential for sustainable and energy-efficient wastewater treatment. Furthermore, the improved performance can be attributed to the synergistic effects of enhanced light absorption, reduced charge recombination, and efficient electron transport, as confirmed by the characterization results. These findings demonstrate that the proposed system is competitive with, and in some aspects advantageous over, existing photocatalytic materials.

4. Conclusion

A visible-light-responsive Bi_2O_3-Er_2O_3/graphene oxide (GO) nanocomposite photocatalyst was successfully synthesized and evaluated. The purpose was to evaluate it for the degradation of metronidazole (MNZ) in aqueous solution. Complete structural, morphological, and optical characterizations proved the uniform anchoring of Bi_2O_3-Er_2O_3 nanoparticles on GO sheets. That caused improved light absorption and efficient suppression of electron-hole recombination. The composite containing 20 wt% GO showed the highest photocatalytic activity. That sample achieved near-complete MNZ degradation when exposed to visible-light. The superior performance was explained by many cooperative effects. Those include Bi_2O_3 -induced visible-light activation. The charge trapping and energy conversion assisted by Er_2O_3 were factors. The excellent electron-transport capability of GO also contributed. Parametric studies showed that alkaline pH, moderate catalyst loading, and lower initial MNZ concentrations favored higher degradation efficiency. Additionally, the optimized photocatalyst showed good stability and reusability during many cycles. These results stress the potential of Bi_2O_3-Er_2O_3/GO nanocomposites as efficient and sustainable photocatalysts for the removal of antibiotic contaminants from wastewater using solar-driven processes.

CRedit Author Statement

Author Contributions: Usama A. Saed: Conceptualization, Methodology, Investigation, Resources, and Data Curation, Writing, Supervision; Nada D. Ali: Conceptualization, Methodology, Formal Analysis, Data Curation; Waqar A. Abdulnabi: Validation, Data Curation; Zeyad Zeitoun: Writing, Review and Editing, Supervision. All authors have read and agreed to the published version of the manuscript. All authors have read and agreed to the published version of the manuscript.

References

[1] Tiwari, B., Sellamuthu, B., Ouarda, Y., Drogui, P., Tyagi, R.D., Buelna, G. (2017) Review on fate and mechanism of removal of pharmaceutical pollutants from wastewater using biological approach, *Bioresource Technology*, 224, 1-12, DOI: 10.1016/j.biortech.2016.11.042.

[2] Edwards, D.I. (1980) Mechanisms of selective toxicity of metronidazole and other nitroimidazole drugs, *Sexually Transmitted Infections*, 56 (5), 285-290, DOI: 10.1136/sti.56.5.285.

[3] Boumahdi, N., Hadj-Ziane-Zafour, A., Yaiche-Achour, H., Khalaf, H. (2022) Preparation of Bi2O3/TiO2–Montmorillonite Nanocomposites and Their Applications to the Photodegradation of Pentachlorophenol, *Bulletin of Chemical Reaction Engineering & Catalysis*, 17 (1), 78-87, DOI: 10.9767/bcrec.17.1.12421.78-87.

[4] Zeitoun, Z., El-Shazly, A.H., Nosier, S., Elmarghany, M.R., Salem, M.S., Taha, M.M. (2020) Performance Evaluation and Kinetic Analysis of Photocatalytic Membrane Reactor in Wastewater Treatment, *Membranes*, 10(10), 276, DOI: 10.3390/membranes10100276

[5] Zeitoun, Z., Selem, N.Y. (2023) A comprehensive review on textile wastewater treatment by coupling TiO2 with PVDF membrane, *Bulletin of the National Research Centre*, 47(1), 153, DOI: 10.1186/s42269-023-01131-9.

[6] Bhatia, A., Hautier, G., Nilgianskul, T., Miglio, A., Sun, J., Kim, H.J., Kim, K.H., Chen, S., Rignanese, G.-M., Gonze, X., Suntivich, J. (2016) High-mobility bismuth-based transparent p-type oxide from high-throughput material screening, *Chemistry of Materials*, 28, (1), 30-34, DOI: 10.1021/acs.chemmater.5b03794.

[7] He, G., Huang, J., Liu, W., Wang, X., Chen, H., Sun, X. (2012) ZnO–Bi2O3/graphene oxide photocatalyst with high photocatalytic performance under visible light, *Materials Technology*, 27 (4), 278-283, DOI: 10.1179/1753555712Y.0000000024.

[8] Bilici, Z., Guler, P., Ozay, Y., Yilmaz, S., Yatmaz, H.C., Dizge, N. (2021) Photocatalytic activity of (Er2O3) x (Yb2O3) y (Bi2O3) 1-xy ternary compounds used as heterogeneous semiconductor, *Materials Science and Engineering: B*, 271, 115250, DOI: 10.1016/j.mseb.2021.115250.

[9] Negash, A., Derseh, L. M., Tedla, A., Yassin, J. M. (2024) Eco-friendly synthesis of CuO/Bi2O3 nanocomposite for efficient photocatalytic degradation of Rhodamine B dye, *Scientific Reports*, 14 (1), 23393, DOI: 10.1038/s41598-024-74408-2.

[10] Sun, D., Zhu, S., Ji, Z., Chen, X., Wu, J., Liu, H., Ling, Y., Hosseini-Bandegharaei, A., Li, Z., Liu, Q. (2025) Construction of Er2O3/ZnIn2S4 heterojunction with enhanced oxygen vacancies and upconversion luminescence property for photocatalytic CO2 reduction, *Fuel*, 400, 135791, DOI: 10.1016/j.fuel.2025.135791.

[11] Lu, K.-Q., Li, Y.-H., Tang, Z.-R., Xu, Y.-J. (2021) Roles of graphene oxide in heterogeneous photocatalysis, *ACS Materials Au*, 1 (1), 37-54, DOI: 10.1021/acsmaterialsau.1c00022.

[12] Ani, P.C., Zeitoun, Z., Al-Abedi, H.J., Smith, J. D. (2026) Graphene Synthesis: A Reactor-Oriented Review of Conventional and Emerging Production Methods, *Chemical Engineering and Processing-Process Intensification*, 22, 110752, DOI: 10.1016/j.cep.2026.110752.

[13] Ani, P.C., Al-Abedi, H.J., Smith, J.D., Zeitoun, Z. (2025). Comparative Morphological and Thermal Analysis of Biochar from Oak, and from Oak, Pine and RDF Blends, in a Downdraft Gasifier, *Fuels*, 6 (3), 73, DOI: 10.3390/fuels6030073.

[14] Ani, P.C., Alhameedi, H., Al-Abedi, H.J., Al-Rubaye, H., Zeitoun, Z., Ewuzie, U., Smith, J.D. (2025) The Comprehensive Quantification and Characterization of Oak Biochar Produced via a Gasification Process Using a Downdraft Reactor, *Fuels*, 6 (3), 51, DOI: 10.3390/fuels6030051.

[15] Cole, T., Ani, P., Jasim, A., Zeitoun, Z., Smith, J. (2025). Process intensification in reverse flow reactors to boost various industrial applications: A review, *Chemical Engineering and Processing-Process Intensification*, 208, 110097, DOI: 10.1016/j.cep.2024.110097.

[16] Saed, U.A., Ali, A.H., Saoud, A.A., Zeitoun, Z. (2025) Enhanced Adsorption of Brilliant Green Dye Using Barium Ferrite/Graphene Oxide Nanocomposites, *Bulletin of Chemical Reaction Engineering & Catalysis*, 20 (4), 683-693, DOI: 10.9767/bcrec.20453.

[17] Rajaji, U., Manavalan, S., Chen, S.-M., Chinnapaiyan, S., Chen, T.-W., Ramalingam, R.J. (2019) Facile synthesis and characterization of erbium oxide (Er2O3) nanospheres embellished on reduced graphene oxide nanomatrix for trace-level detection of a hazardous pollutant causing Methemoglobinaemia, *Ultrasonics Sonochemistry*, 56, 422-429, DOI: 10.1016/j.ultsonch.2019.02.023.

[18] Astuti, Y., Elesta, P.P., Widodo, D.S., Widiyandari, H., Balgis, R. (2020) Hydrazine and urea fueled-solution combustion method for Bi2O3 synthesis: characterization of physicochemical properties and photocatalytic activity, *Bulletin of Chemical Reaction Engineering & Catalysis*, 15 (1), 104-111, DOI: 10.9767/bcrec.15.1.5483.104-111.

[19] Wang, C., Liu, H., Wang, G., Fang, H., Yuan, X., Lu, C. (2022) Photocatalytic removal of metronidazole and Cr (Ⅵ) by a novel Zn3In2S6/Bi2O3 S-scheme heterojunction: Performance, mechanism insight and toxicity assessment, *Chemical Engineering Journal*, 450, 138167, DOI: 10.1016/j.cej.2022.138167.

[20] Yu, C., Dong, S., Feng, J., Hu, L., Li, Y., Sun, J. (2014) Controlled synthesis of uniform BiVO4 microcolumns and advanced visible-light-driven photocatalytic activity for the degradation of metronidazole-contained wastewater, *Environmental Science and Pollution Research*, 21 (4), 2837-2845, DOI: 10.1007/s11356-013-2224-6.

[21] Rahman, M.S., Suvo, M.A.H., Islam, M., Noor, A.R., Yeachin, N., Bhuiyan, M. A. (2024) Fast and efficient removal of metronidazole from aqueous solution using graphene oxide (GO) supported nitrogen (N) doped zinc oxide (ZnO) nanoparticles. *Colloids and Surfaces A: Physicochemical and Engineering Aspects*, 690, 133660, DOI: 10.1016/j.colsurfa.2024.133660.

[22] Vekhande, H.N., Bagawade, J.A. (2026) Synthesis and characterization of graphene oxide using a modified Hummers method for enhanced quality and yield, *Fullerenes, Nanotubes and Carbon Nanostructures*, 34 (3), 251-257, DOI: 10.1080/1536383X.2025.2530136.

[23] Wang, H., Zhang, L., Chen, Z., Hu, J,, Li, S., Wang, Z., Liu, J., Wang, X. (2014) Semiconductor heterojunction photocatalysts: design, construction, and photocatalytic performances, *Chemical Society Reviews*, 43 (15), 5234-5244, DOI: 10.1039/c4cs00126e.

[24] Henderson, M.A. (2011) A surface science perspective on TiO2 photocatalysis, *Surface Science Reports*, 66 (6-7), 185-297, DOI: 10.1016/j.surfrep.2011.01.001.

[25] Kamat, P.V. (2011) Graphene-based nanoassemblies for energy conversion, *The Journal of Physical Chemistry Letters*, 2 (3), 242-251, DOI: 10.1021/jz101639v.

[26] Zhang, N., Zhang, Y., Xu, Y.-J. (2012) Recent progress on graphene-based photocatalysts: current status and future perspectives, *Nanoscale*, 4 (19), 5792-5813, DOI: 10.1039/C2NR31480K.

[27] Li, X., Yu, J., Wageh, S., Al-Ghamdi, A.A., Xie, J. (2016). Graphene in photocatalysis: a review, *Small*, 12 (48), 6640-6696, DOI: 10.1002/smll.201600382.

[28] Yang, P., Yang, X., Liu, W., Guo, R., Yao, Z. (2023) Graphene-based electrocatalysts for advanced energy conversion, *Green Energy & Environment*, 8 (5), 1265-1278, DOI: 10.1016/j.gee.2022.06.008.

[29] Ramalingam, G., Perumal, N., Priya, A., Rajendran, S. (2022) A review of graphene-based semiconductors for photocatalytic degradation of pollutants in wastewater, *Chemosphere*, 300, 134391, DOI: 10.1016/j.chemosphere.2022.134391.

[30] Khan, A.U.R., Ramzan, M., Alanazi, S.J.F., Al-Mohaaimeed, A.M., Ali, S., Imran, M., Majid, M.A., Sarfraz, M.H. (2024) Structural, Optical, Electrical and Photocatalytic Investigation of n-Type Zn2+-Doped α-Bi2O3 Nanoparticles for Optoelectronics Applications, *ACS Omega*, 9 (21), 22650-22659, DOI: 10.1021/acsomega.3c10521.

[31] Williams, D.B., Carter, C.B. (1999) Transmission electron microscopy-A textbook for materials science, Vol. 1, Second Edition, Springer.

[32] Thiruppathi, A.R., Sidhureddy, B., Boateng, E., Soldatov, D.V., Chen, A. (2020) Synthesis and electrochemical study of three-dimensional graphene-based nanomaterials for energy applications, *Nanomaterials*, 10 (7), 1295, DOI: 10.3390/nano10071295.

[33] El-Khair, M.A.A., Abo El Naga, A.O., Elwakeel, K.Z., Elgarahy, A.M., Priya, A.K., Yadav, K.K., Morshedy, A.S. 2025) The promise of graphene-based photocatalytic materials for wastewater remediation: A scoping review, *Coordination Chemistry Reviews*, 544, 216961, DOI: 10.1016/j.ccr.2025.216961.

[34] Dreyer, D.R., Park, S., Bielawski, C.W., Ruoff, R.S. (2010) The chemistry of graphene oxide, *Chemical Society Reviews*, 39 (1), 228-240, DOI: 10.1039/B917103G.

[35] Tale, B., Nemade, K., Tekade, P. (2021) Graphene based nano-composites for efficient energy conversion and storage in Solar cells and Supercapacitors: A Review, *Polymer-Plastics Technology and Materials*, 60 (7), 784-797, DOI: 10.1080/25740881.2020.1851378.

[36] Jafari, E., Tamimzadeh, A., Farhadian, M., Nazar, A.R.S. (2025) Visible-light photocatalytic degradation of metronidazole using an S-scheme amino acid glycine–modified TiO2/Fe3O4 heterojunction immobilized on chitosan–Polyacrylonitrile in a batch Photoreactor, *International Journal of Biological Macromolecules*, 328, Part. 1, 147442, DOI: 10.1016/j.ijbiomac.2025.147442.

[37] Lykos, C., Kourkouta, T., Konstantinou, I. (2023) Study on the photocatalytic degradation of metronidazole antibiotic in aqueous media with TiO2 under lab and pilot scale, *Science of The Total Environment*, 870, 161877, DOI: 10.1016/j.scitotenv.2023.161877.

[38] Bagum, M., Islam, S., Khan, E.A., Khandaker, J.I., Ahmed, F. (2023) Degradation of Metronidazole from Aqueous Environment Using Hydrothermally Synthesized ZnO, N-Doped ZnO, and ZnO/AC Nanoparticles, *Advances in Condensed Matter Physics*, 2023 (1), 8706698, DOI: 10.1155/2023/8706698.

[39] Al-Gheethi, A., Sundram, N., Crane, R., Alburihi, A., Maya, R., Mohamed, S.R., Al-Shaibani, M.M., Noman, E.A., Ponnusamy, S.K., Kamil, N.A.F.M. (2022) Metronidazole photocatalytic degradation by zinc oxide nanoparticles synthesized in watermelon peel extract; advanced optimization, simulation and numerical models using machine learning applications, *Environmental Research*, 212, 113537, DOI: 10.1016/j.envres.2022.113537.

[40] Yeganeh, M., Sobhi, H.R., Esrafili, A. (2022) Efficient photocatalytic degradation of metronidazole from aqueous solutions using Co/g-C3N4/Fe3O4 nanocomposite under visible light irradiation, *Environmental Science and Pollution Research*, 29 (17), 25486-25495, DOI: 10.1007/s11356-021-17077-2.

[41] Yazdanpanah, G., Heidari, M.R., Amirmahani, N., Nasiri, A. (2023) Heterogeneous Sono-Fenton like catalytic degradation of metronidazole by Fe3O4@ HZSM-5 magnetite nanocomposite, *Heliyon*, 9 (6), DOI: 10.1016/j.heliyon.2023.e16461.